# Doped Organic Semiconductors for Infrared Detection

Supplementary material

BIJNENS, Bram; GIELEN, Sam; MAES, Wouter & VANDEWAL, Koen (2025) Doped Organic Semiconductors for Infrared Detection. In: Advanced functional materials, (Art N° e14973).

DOI: 10.1002/adfm.202514973
Handle: http://hdl.handle.net/1942/47433

ADVANCED FUNCTIONAL MATERIALS

# Supporting Information

for *Adv. Funct. Mater.*, DOI 10.1002/adfm.202514973

Doped Organic Semiconductors for Infrared Detection

*Bram Bijnens*, Sam Gielen, Wouter Maes and Koen Vandewal**

WILEY-VCH

# Supporting Information

## Doped Organic Semiconductors for Infrared Detection

*Bram Bijnens*, Sam Gielen, Wouter Maes, Koen Vandewal**

B. Bijnens, S. Gielen, W. Maes, K. Vandewal
Hasselt University, Institute for Materials Research (imo-imomec), Martelarenlaan 42, B-3500 Hasselt, Belgium
E-mail: bram.bijnens@uhasselt.be, koen.vandewal@uhasselt.be

B. Bijnens, S. Gielen, W. Maes, K. Vandewal
imec, imo-imomec, Wetenschapspark 1, B-3590 Diepenbeek, Belgium
E-mail: bram.bijnens@uhasselt.be, koen.vandewal@uhasselt.be

**Contents**

## S1 Samples

The samples consist of five layers, of which two are sacrificial. The real devices are lifted off the sacrificial layers, resulting in extremely thin devices (in the order of 100ths of nm to a few µm).

The first sacrificial layer is the glass substrate, with a thickness of 1 mm. Using a glass substrate would significantly disadvantage the device's performance because of the added thickness. Still, the purpose is very straightforward: all the typical fabrication steps and setups can be used by using a sacrificial glass substrate. The second sacrificial layer is a layer of polyethylene glycol (PEG) with a thickness of 200 nm; its only purpose is to detach the actual device from the glass in a easier fashion.

For the actual device, the substrate is a parylene-C layer, the thickness of which is varied between 250-4000 nm, resulting in a flexible device. This variation in the thickness of the parylene-C allows us to investigate the influence of device thickness without drastically increasing or decreasing the absorption. Three different host:dopant systems are used as the organic absorbing layer: MeO-TPD:F6TCNNQ, PBiTTQHD:F6TCNNQ, and PEDOT:PSS. This layer is the active layer of the device which absorbs the IR radiation and changes resistance as a consequence of the temperature change. The final layer is the planar metal contacts consisting of silver spaced over distance $L$, which is varied from 50 µm to 1.6 mm.

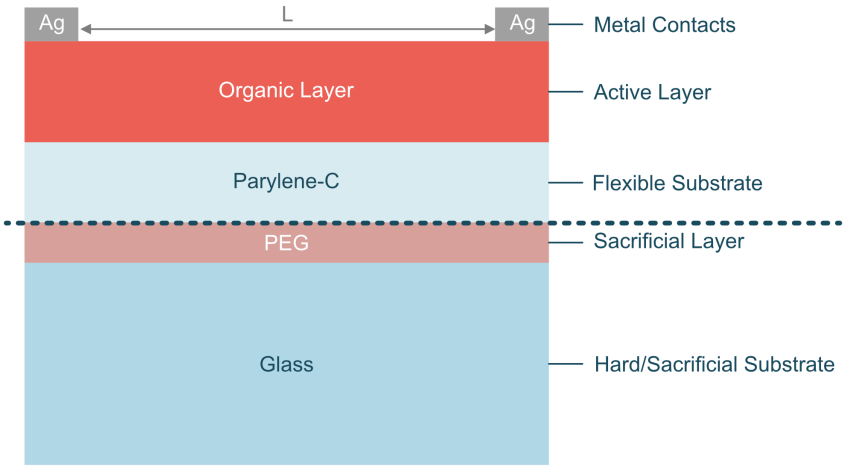


**Figure S1.** Schematic overview of the device structure. The five layers can be divided into the two sacrificial layers and the three layers of the actual device; the blue dashed line indicates the division.

### S1.1 Contacts

After the deposition of the organic layer, the metal contacts are thermally evaporated on top at a rate of 0.5 Å/s for 30 nm and at 1 Å/s for 70 nm, resulting in a total thickness of 100 nm. Two contact layouts were used for the actual bolometer devices and one for the temperature-dependent IV measurements. For the bolometer devices, one has a linear spacing from 200-450 µm inter-contact distance (Figure S2a,e), and a second one with logarithmically spaced contacts from 50 µm-1.6 mm (Figure S2b,f). The 50 µm is often shorted during evaporation due to slight mask movements, and the 1.6 mm spaced contact cells often had too high resistance to be useful. For this reason, the linearly spaced mask from Figure S2e is used. The mask for

the temperature-dependent IV has spacings of 100, 200, 400, and 800 µm (Figure S2c,g). To measure the bolometer devices, a custom holder was designed in which pogo pins are used to connect with the ultra-thin devices.

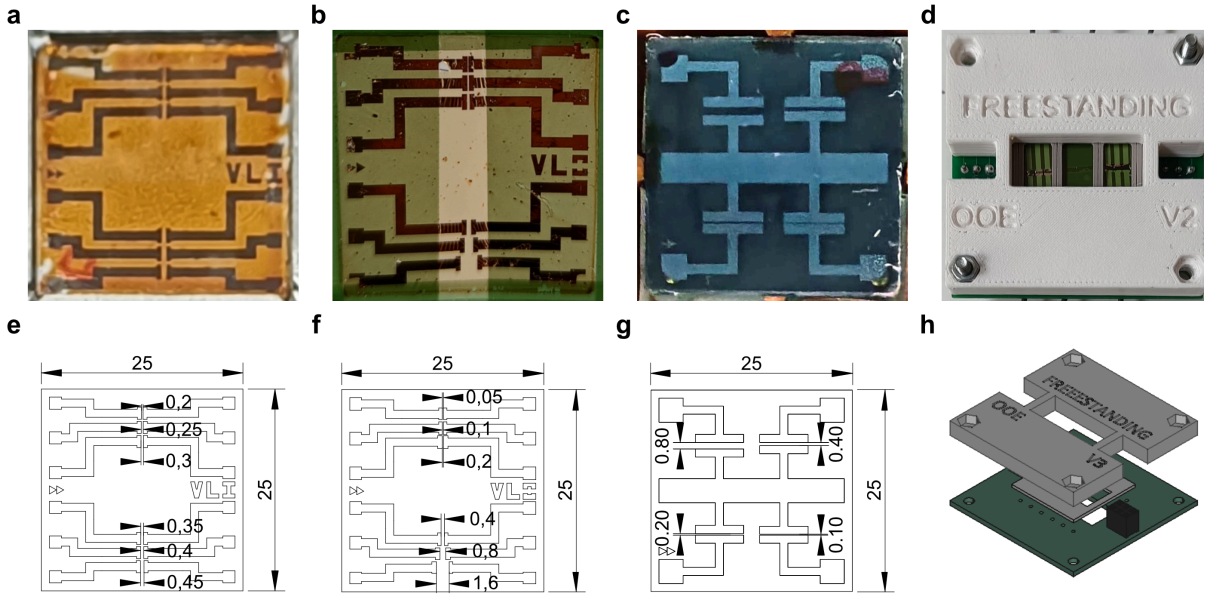


**Figure S2.** (a) An example of a MeO-TPD sample with contacts evaporated using the linearly spaced mask in (e). (b) An example of a PBiTTQHD sample with contacts evaporated using the logarithmically spaced mask as in (f). (c) An example of a PEDOT sample with the contacts for the temperature-dependent IV is shown in (g). (d) Picture of a bolometer sample in the custom-made holder. (e) The linearly spaced mask with varying the contact spacing from 200 to 450 µm. (f) The logarithmically spaced mask varying the contact spacing from 50 µm to 1.6 mm. (g) The mask for the temperature-dependent IV with contact spacings of 100, 200, 400, and 800 µm. (h) A schematic overview of the custom sample holder.

## S2 The Heat Equation

### S2.1 Steady-State Solution

When looking at a simplified model for the bolometer samples, we solve the heat equation accounting for four terms: the heat conduction term, the radiation term, the convection term, and the absorbed energy term, given by:

$$\frac{\partial T}{\partial t} = \frac{k}{c_s \rho}\frac{\partial^2 T}{\partial x^2} - \frac{\varepsilon \sigma_{\mathrm{SB}}}{c_s \rho d}\left(T^4 - T_{\mathrm{b}}^4\right) - \frac{\gamma}{c_s \rho d}(T - T_b) + \frac{Q_A}{c_s \rho d} \tag{S1}$$

with $T$ the temperature (K), $k$ the thermal conductivity (W/mK), $c_s$ the specific heat capacity (J/kgK), $\rho$ the density (kg/m³), $\varepsilon$ the emissivity, $\sigma_{\mathrm{SB}}$ the Stefan-Boltzmann constant ($5.67 \cdot 10^{-8}$ W/m²K⁴), $d$ the thickness of the device (m), $\gamma$ the heat transfer coefficient for convection (W/m²K), and $Q_A$ the absorbed energy (W/m²). When assuming small temperature changes, the equation can be simplified to:

$$\begin{aligned}
\frac{\partial \Delta T}{\partial t} &= \frac{k}{c_s \rho}\frac{\partial^2 \Delta T}{\partial x^2} - 4T_b^3\frac{\varepsilon \sigma_{\mathrm{SB}}}{c_s \rho d}\Delta T + \mathcal{O}(\Delta T^2) - \frac{\gamma}{c_s \rho d}\Delta T + \frac{Q_A}{c_s \rho d} \\
\frac{\partial \Delta T}{\partial t} &= \frac{k}{c_s \rho}\frac{\partial^2 \Delta T}{\partial x^2} - \frac{4T_b^3\varepsilon \sigma_{\mathrm{SB}} + \gamma}{c_s \rho d}\Delta T + \frac{Q_A}{c_s \rho d} \\
\frac{\partial \Delta T}{\partial t} &= A\frac{\partial^2 \Delta T}{\partial x^2} - B\Delta T + C
\end{aligned} \tag{S2}$$

Now, we solve Equation S2 under steady-state conditions (where $\partial \Delta T / \partial t = 0$):

$$\begin{aligned}
A\frac{\partial^2 \Delta T}{\partial x^2} &= B\Delta T - C \\
\frac{\partial^2 \Delta T}{\partial x^2} &= \frac{B}{A}\Delta T - \frac{C}{A}
\end{aligned} \tag{S3}$$

The solution to Equation S3 is:

$$\Delta T(x) = \frac{C}{B} + \Gamma_1 e^{\sqrt{B/A}\,x} + \Gamma_2 e^{-\sqrt{B/A}\,x}$$

We take the center of the domain at $x = 0$ and thus the contacts at $x = \pm L/2$. Combining this with the assumption that the contacts are metallic and thus perfect heatsinks, the following boundary conditions apply:

$$\begin{cases} \dfrac{\partial \Delta T}{\partial x}\Big|_{x=0} = 0 \\[2ex] \Delta T|_{x=L/2} = 0 \end{cases}$$

Differentiating Equation S3, we get:

$$\frac{\partial \Delta T}{\partial t}\Big|_{x=0} = 0 = \Gamma_1\sqrt{\frac{B}{A}} - \Gamma_2\sqrt{\frac{B}{A}} \Rightarrow \Gamma_1 = \Gamma_2 = \frac{\Gamma}{2}$$

Plugging this back into Equation S3:

$$\Delta T(x) = \frac{C}{B} + \Gamma \, \frac{e^{\sqrt{\frac{B}{A}}\, x} + e^{-\sqrt{\frac{B}{A}}\, x}}{2} = \frac{C}{B} + \Gamma \cosh\left(\sqrt{A_2}\, \frac{L}{2}\right) \tag{S4}$$

Then, using the second boundary condition:

$$\Delta T|_{x=L/2} = 0 = \frac{C}{B} + \Gamma \cosh\left(\sqrt{\frac{B}{A}}\, \frac{L}{2}\right)$$

$$\Gamma = -\frac{C}{B \cosh\left(\sqrt{\frac{B}{A}}\, \frac{L}{2}\right)} \tag{S5}$$

And if we fill in Equation S5 into Equation S4, we get the final solution:

$$\Delta T(x) = \frac{C}{B} + \Gamma \cosh\left(\sqrt{\frac{B}{A}}\, x\right)$$

$$\Delta T(x) = \frac{C}{B}\left(1 - \frac{\cosh\left(\sqrt{\frac{B}{A}}\, x\right)}{\cosh\left(\sqrt{\frac{B}{A}}\, \frac{L}{2}\right)}\right) \tag{S6}$$

Examples of the heat profiles in function of $x$ for various $L$ are shown in Figure S3, where it is clear that the larger $L$ gets, the closer $\Delta T$ comes to a limiting value. We can calculate a maximal amplitude that we reach in the radiation-limited case. This means that we look at two cases: one in a vacuum ($\gamma = 0$) and one more realistic for the situation in ambient atmosphere, where we assume the heat transfer due to convection is equally important as the heat transfer due to radiation ($\gamma = 4T_b^3 \varepsilon \sigma_{\mathrm{SB}}$):

$$\Delta T_{\max} = \frac{C}{B} \tag{S7}$$

$\gamma = 0$

$$\begin{aligned}
\Delta T_{\max} &= \frac{\frac{Q_A}{c_s \rho d}}{\frac{4T_b^3 \varepsilon \sigma_{\mathrm{SB}} + \gamma}{c_s \rho d}} \\
&= \frac{Q_A}{4T_b^3 \varepsilon \sigma_{\mathrm{SB}} + 0} \\
&= \frac{Q_A}{4\varepsilon \sigma_{\mathrm{SB}} T_b^3} \\
&\approx \frac{1 \frac{\mathrm{W}}{\mathrm{m}^2}}{4 \cdot 1 \cdot 5.67 \cdot 10^{-8} \frac{\mathrm{W}}{\mathrm{m}^2 \mathrm{K}^4} \cdot (300\mathrm{K})^3} \\
\Delta T_{\max} &\approx 0.163 \text{ K}
\end{aligned}$$

$\gamma = 4T_b^3 \varepsilon \sigma_{\mathrm{SB}}$

$$\begin{aligned}
\Delta T_{\max} &= \frac{\frac{Q_A}{c_s \rho d}}{\frac{4T_b^3 \varepsilon \sigma_{\mathrm{SB}} + \gamma}{c_s \rho d}} \\
&= \frac{Q_A}{4T_b^3 \varepsilon \sigma_{\mathrm{SB}} + 4T_b^3 \varepsilon \sigma_{\mathrm{SB}}} \\
&= \frac{Q_A}{8\varepsilon \sigma_{\mathrm{SB}} T_b^3} \\
&\approx \frac{1 \frac{\mathrm{W}}{\mathrm{m}^2}}{8 \cdot 1 \cdot 5.67 \cdot 10^{-8} \frac{\mathrm{W}}{\mathrm{m}^2 \mathrm{K}^4} \cdot (300\mathrm{K})^3} \\
\Delta T_{\max} &\approx 0.082 \text{ K}
\end{aligned}$$

So the maximal temperature increase we can expect is 0.163 K and 0.082 per W/m² power we put in for vacuum and ambient air, respectively (dark blue horizontal line in Figure S3a).

The average temperature change can be calculated by integrating Equation S6 over the spacing between the contacts:

$$
\begin{aligned}
\Delta T_{\text{avg}} &= \frac{2}{L}\int_0^{L/2} \Delta T(x)\,\mathrm{d}x \\
&= \frac{2}{L}\int_0^{L/2} \frac{C}{B}\left(1 - \frac{\cosh\left(\sqrt{\frac{B}{A}}\,x\right)}{\cosh\left(\sqrt{\frac{B}{A}}\,\frac{L}{2}\right)}\right)\mathrm{d}x \\
&= \frac{2}{L}\frac{C}{B}\left[\int_0^{L/2} 1\;\mathrm{d}x - \frac{1}{\cosh\left(\sqrt{\frac{B}{A}}\,\frac{L}{2}\right)}\int_0^{L/2}\cosh\left(\sqrt{\frac{B}{A}}\,x\right)\mathrm{d}x\right] \\
&= \frac{2}{L}\frac{C}{B}\left[\frac{L}{2} - \frac{1}{\sqrt{\frac{B}{A}}}\frac{\sinh\left(\sqrt{\frac{B}{A}}\,\frac{L}{2}\right)}{\cosh\left(\sqrt{\frac{B}{A}}\,\frac{L}{2}\right)}\right] \\
\Delta T_{\text{avg}} &= \frac{C}{B}\left[1 - \frac{2}{L\sqrt{\frac{B}{A}}}\tanh\left(\sqrt{\frac{B}{A}}\,\frac{L}{2}\right)\right]
\end{aligned}
\tag{S8}
$$

The average temperature increase has the same theoretical limits of 0.163 K and 0.082 K per W/m² (Figure S3b). This maximum temperature increase is achieved when the contact spacing, $L$, is significantly larger than $\sqrt{kd}$, which is equivalent to the condition that $\sqrt{kd}/L$ is small, as illustrated in Figure S4.

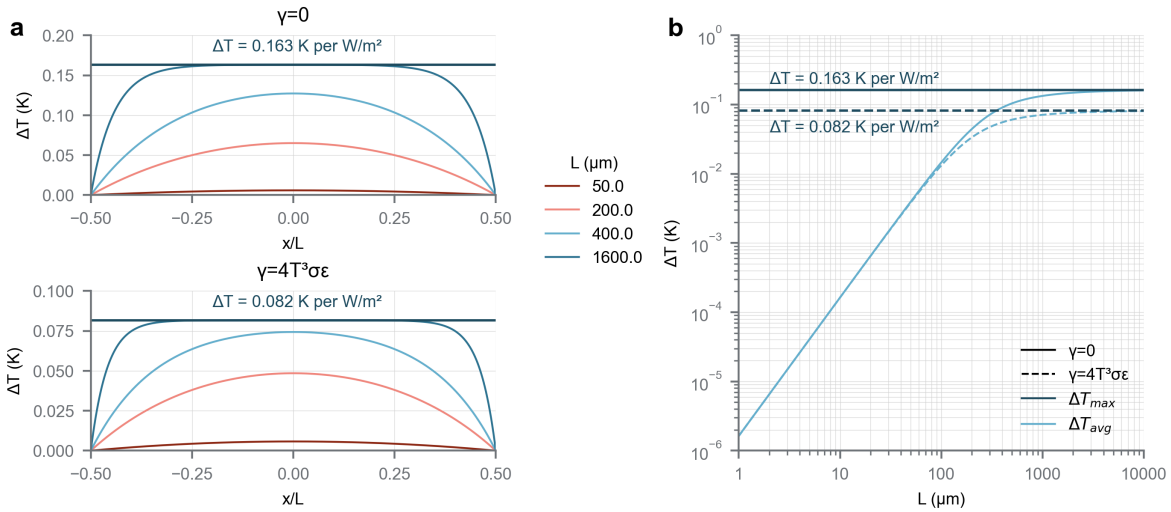


**Figure S3.** (a) The x-profile of the temperature increase ($\Delta T$) for various electrode spacings ($L$). This graph shows that for larger electrode distances, we reach the theoretical limit of ($\Delta T_{\text{max}}$) of 0.163 and 0.082 K per W/m² (the dark blue horizontal line) for $\gamma = 0$ and $\gamma = 4T_b^3\sigma_{\text{SB}}\varepsilon$, respectively. The full parameters are shown in Table S1. (b) The average temperature increase ($\Delta T_{\text{avg}}$) in function of the electrode spacing, reaching the expected limits. The full parameter set is shown in Table S1.

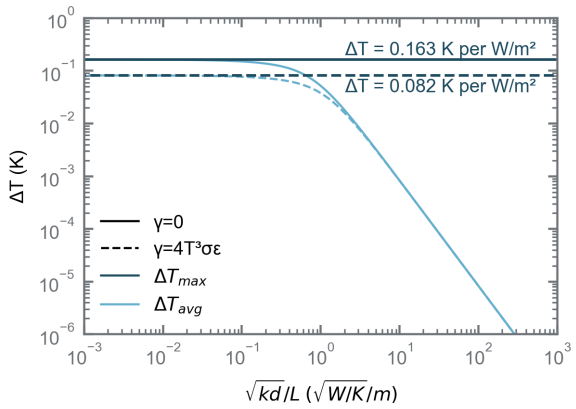


**Figure S4.** The change in temperature, $\Delta T$, as a function of the parameter $\sqrt{kd}/L$. The plot demonstrates that when $\sqrt{kd}/L$ is sufficiently small, the maximum $\Delta T$ is reached, indicating a radiation-limited regime.

**Table S1.** The parameters to use in Equation S6 to reproduce the results in Fig. 1a in the main text and Figure S3.

| **Parameter** | **Value** |
|---|---|
| $T_b$ | 300 K |
| $d_o$ | 100 nm |
| $d_p$ | 250 nm |
| $d$ | $d_o + d_p$ = 350 nm |
| $k_o$ | 0.3 W/mK |
| $k_p$ | 0.084 W/mK |
| $k$ | $k_o \frac{d_o}{d} + k_p \frac{d_p}{d}$ = 0.1457 W/mK |
| $\sigma_{\mathrm{SB}}$ | $5.67 \cdot 10^{-8}$ W/m²K⁴ |
| $L$ | 50 µm, 200 µm, 400 µm, 1600 µm |
| $\rho$ | 1100 kg/m³ |
| $c_s$ | 770 J/kgK |
| $\gamma$ | 0 W/m²K or $4\varepsilon\sigma_{\mathrm{SB}}T_b^3$ = 6.12 W/m²K |
| $Q_A$ | 1 W/m² |
| $\varepsilon$ | 1 |

### S2.2 Time-dependent Solution

When the incoming radiation is modulated, for example with a chopper the solution of the heat equation becomes time-dependent. To model this, we change the energy input from $Q_A$ to $Q_A e^{-i2\pi ft}$ where $f$ is the chopper frequency. So the heat equation becomes:

$$\frac{\partial T}{\partial t} = \frac{k}{c_s \rho}\frac{\partial^2 T}{\partial x^2} - \frac{\varepsilon \sigma_{\mathrm{SB}}}{c_s \rho d}\left(T^4 - T_{\mathrm{b}}^4\right) - \frac{\gamma}{c_s \rho d}(T - T_b) + \frac{Q_A}{c_s \rho d}e^{-i2\pi ft}$$

$$\frac{\partial \Delta T}{\partial t} = A\frac{\partial^2 \Delta T}{\partial x^2} - B\Delta T + Ce^{-i2\pi ft}$$

Now, we can assume that the solution will also be periodical with the same periodicity $\left(\Delta T(x,t) = \Delta T(x)e^{-i2\pi ft}\right)$:

$$\Delta T(x)\frac{\partial e^{-i2\pi ft}}{\partial t} = Ae^{-i2\pi ft}\frac{\partial^2 \Delta T(x)}{\partial x^2} - Be^{-i2\pi ft}\Delta T(x) + Ce^{-i2\pi ft}$$

$$\Delta T(x)(-i2\pi f)e^{-i2\pi ft} = Ae^{-i2\pi ft}\frac{\partial^2 \Delta T(x)}{\partial x^2} - Be^{-i2\pi ft}\Delta T(x) + Ce^{-i2\pi ft}$$

$$\Delta T(x)(-i2\pi f) = A\frac{\partial^2 \Delta T(x)}{\partial x^2} - B\Delta T(x) + C$$

$$\frac{\partial^2 \Delta T(x)}{\partial x^2} = \frac{B - i2\pi f}{A}\Delta T(x) - \frac{C}{A}$$

This leads to the partial differential equation in Equation S3, so the solution will again be Equation S6 and the average Equation S8, the only the difference is that $A_2$ becomes a complex number:

$$\frac{B}{A} \Rightarrow \frac{B - i2\pi f}{A}$$

So, the time-dependent solution is:

$$\Delta T(x,f,t) = \frac{C}{B - i2\pi f}\left(1 - \frac{\cosh\left(\sqrt{\frac{B-i2\pi f}{A}}\ x\right)}{\cosh\left(\sqrt{\frac{B-i2\pi f}{A}}\ \frac{L}{2}\right)}\right)e^{-i2\pi ft} \tag{S9}$$

This means the maximal temperature difference for the thermally limited case becomes:

$$\begin{aligned}\Delta T_{\max}(f) &= \left|\frac{C}{B - i2\pi f}\right| \\ &= \sqrt{\frac{C^2}{B^2 + 4\pi^2 f^2}} \\ &= \frac{C}{\sqrt{B^2 + 4\pi^2 f^2}}\end{aligned} \tag{S10}$$

### S2.3 Cutoff Frequency and Response Time

We define the cutoff frequency ($f_{3\mathrm{dB}}$) as the frequency where the amplitude is $1/\sqrt{2}$ times the maximal amplitude, which is by $f = 0$.

$$\frac{1}{\sqrt{2}}\frac{C}{B} = \frac{C}{\sqrt{B^2 + 4\pi^2 f_{3\mathrm{dB}}^2}}$$

$$B^2 + 4\pi^2 f_{3\mathrm{dB}}^2 = 2B^2$$

$$f_{3\mathrm{dB}} = \frac{B}{2\pi}$$

| $\gamma = 0$ | $\gamma = 4T_b^3 \varepsilon \sigma_{\mathrm{SB}}$ |
|---|---|
| $f_{3\mathrm{dB}} = \frac{2T_b^3 \varepsilon \sigma_{\mathrm{SB}}}{\pi c_s \rho d}$ | $f_{3\mathrm{dB}} = \frac{4T_b^3 \varepsilon \sigma_{\mathrm{SB}}}{\pi c_s \rho d}$ |
| $\approx \frac{2 \cdot (300\ \mathrm{K})^3 \cdot 1 \cdot 5.67 \cdot 10^{-8} \frac{\mathrm{W}}{\mathrm{m^2 K^4}}}{\pi \cdot 1100 \frac{\mathrm{kg}}{\mathrm{m^3}} \cdot 770 \frac{\mathrm{J}}{\mathrm{kgK}} \cdot 1500 \cdot 10^{-9}\ \mathrm{m}}$ | $\approx \frac{2 \cdot (300\ \mathrm{K})^3 \cdot 1 \cdot 5.67 \cdot 10^{-8} \frac{\mathrm{W}}{\mathrm{m^2 K^4}}}{\pi \cdot 1100 \frac{\mathrm{kg}}{\mathrm{m^3}} \cdot 770 \frac{\mathrm{J}}{\mathrm{kgK}} \cdot 1500 \cdot 10^{-9}\ \mathrm{m}}$ |
| $\approx 0.77\ \mathrm{Hz}$ | $\approx 1.53\ \mathrm{Hz}$ |

To calculate the response time:

$$\tau = \frac{1}{2\pi f_{3\mathrm{dB}}} = \frac{1}{B} = \frac{c_S \rho}{4T_b^3 \varepsilon \sigma_{\mathrm{SB}} + \gamma} d \tag{S11}$$

| $\gamma = 0$ | $\gamma = 4T_b^3 \varepsilon \sigma_{\mathrm{SB}}$ |
|---|---|
| $\tau = \frac{1}{2\pi \cdot 0.77\ \mathrm{Hz}}$ | $\tau = \frac{1}{2\pi \cdot 1.53\ \mathrm{Hz}}$ |
| $= 207\ \mathrm{ms}$ | $= 104\ \mathrm{ms}$ |

From Equation S11 we see that the response time is proportional to the thickness when the heat only dissipates from radiation and not from conduction.

### S2.4 Influence of Thermal Conductivity

When the thermal conductivity is increased, the heat is transferred faster, resulting in a smaller difference between the frequency response of different thicknesses. This is shown in Figure S5, where the difference between the response is clear for all thicknesses when $k$ is 0.001 W/mK. Increasing $k$ to 0.01 W/mK it becomes hard to distinguish the difference between 1500, 2000, and 2500 nm. For a $k$ of 0.1 W/mK only the 500 nm is clearly separated from the other thicknesses.

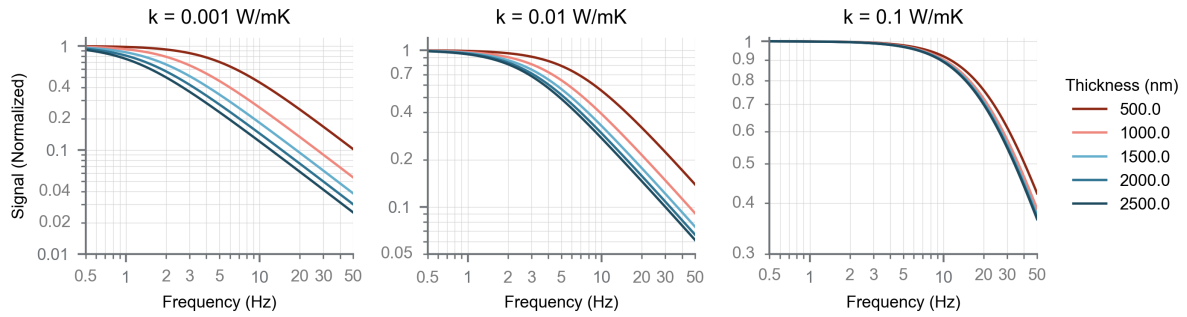


**Figure S5.** The frequency response for a $k$ of 0.001, 0.01, and 0.1 W/mK, respectively. The difference between the thicknesses becomes less pronounced when $k$ is increased.

## S3 Detectivity Calculations

### S3.1 Thermally Limited Detectivity

To derive the formula for the thermally limited specific detectivity, we must start with the fundamental and defining the heat conductance ($G$) as the factor relating the temperature difference ($\Delta T$) to the heat load ($P$) (This section is based on [27]):

$$G = \frac{P}{\Delta T} \tag{S12}$$

From thermodynamics we know the following relation for the expected value of a perturbed property of the body ($l$) with relation the entropy ($S$):

$$\left\langle \left(l - \bar{l}\right)^2 \right\rangle = -\frac{k_B}{\frac{\partial^2 S}{\partial l^2}}$$

with $\bar{l}$ the average of $l$ and $k_B$ the Boltzmann constant. Now, taking the property to be the temperature ($l = T$)

$$\left\langle \Delta T^2 \right\rangle = -\frac{k_B}{\frac{\partial^2 S}{\partial T^2}}$$

and,

$$\frac{\partial S}{\partial T} = \left(\frac{1}{T}\frac{\partial Q}{\partial T}\right) = \frac{C}{T}$$

$$\frac{\partial^2 S}{\partial T^2} = \frac{\partial\left(\frac{C}{T}\right)}{\partial T} = -\frac{C}{T^2}$$

where $Q$ is the heat and $C$ is the heat capacity. So,

$$\Delta T^2 = -k_B\left(-\frac{T^2}{C}\right) = \frac{k_B T^2}{C}$$

For electronic devices, the responsivity ($S$) is:

$$S = \frac{S_0}{1 + i2\pi f\tau}$$

where $S_0$ is the DC responsivity, $f$ the modulation frequency, and $\tau$ the response time:

$$S_0 = \frac{\varepsilon|\zeta|}{G}$$

where $\varepsilon$ is the emissivity, $\zeta = \alpha U$, $\alpha = \frac{1}{R}\frac{\mathrm{d}R}{\mathrm{d}T}$ is the temperature coefficient of resistance and $G$ the thermal conductance. The bandwidth ($\Delta f$) is defined as:

$$\Delta f = \int_0^\infty \left|\frac{S}{S_0}\right|^2 \mathrm{d}f = \int_0^\infty \frac{\mathrm{d}f}{1 - (2\pi f\tau)^2} = \frac{1}{4\tau}$$

Usually the squared noise equivalent power ($N$) is considered per unit bandwidth, which is called NEP:

$$\mathrm{NEP}^2 = \frac{N^2}{\Delta f}$$

If we now look at the thermal conductance:

$$G^2 = \frac{\Delta P^2}{\Delta T^2} = \frac{\mathrm{NEP}^2 \Delta f}{\Delta T^2}$$

The response time defines the characteristic time for the heat transfer:

$$\tau = \frac{C}{G} = \frac{C}{HA}$$

where $H$ is the heat transfer. To calculate the NEP:

$$\begin{aligned}
\mathrm{NEP}^2 &= \frac{G^2 \Delta T^2}{\Delta f} \\
&= \frac{G^2}{\Delta f} \frac{k_B T^2}{C} \\
&= \frac{G^2}{\frac{1}{4\tau}} \frac{k_B T^2}{C} \\
&= \frac{G^2}{\frac{1}{4}\frac{G}{C}} \frac{k_B T^2}{C} \\
\mathrm{NEP}^2 &= 4 G k_B T^2 \qquad \text{(S13)}
\end{aligned}$$

The detectivity is defined as:

$$\begin{aligned}
D^\star_{\mathrm{Tel}} &= \frac{\sqrt{A}}{\mathrm{NEP}} \\
&= \frac{\sqrt{A}}{2T\sqrt{G k_B}} \\
&= \frac{1}{2T}\sqrt{\frac{\tau A}{k_B C}} \\
&= \frac{1}{2T}\sqrt{\frac{\tau A}{k_B c_s \rho V}} \\
&= \frac{1}{2T}\sqrt{\frac{\tau}{k_B c_s \rho d}} \qquad \text{(S14)} \\
D^\star_{\mathrm{Tel}} &= \frac{1}{2T}\frac{1}{\sqrt{k_B H}} \qquad \text{(S15)}
\end{aligned}$$

and we can also define $D^\star_T = \varepsilon D^\star_{\mathrm{Tel}}$.

### S3.2 Jones Limit

The heat transfer consists of three parts: $H_R$, the heat transfer by radiation, $H_C$, the heat transfer by conduction, and $H_P$ the heat transfer by parasitic heat flows:

$$H = H_R + H_C + H_P$$

To achieve the upper limit of detectivity, known as the Jones limit, the heat transfer coefficient $H$ must be minimized. This indicates that there should be no convection, resulting in $H_C = 0$. Additionally, the material must function as a perfect thermal insulator with no unwanted heat transfer, which implies that $H_P = 0$. As a result, the total heat transfer occurs solely through radiation, leading to $H = H_R$. According to the Stefan-Boltzmann law, we can express $H_R$ as follows:

$$H_R = 4\varepsilon\sigma_{\mathrm{SB}}T^3$$

Plugging this back into Equation S15:

$$\begin{aligned} D^\star_{\mathrm{J}} &= \frac{\varepsilon}{2T}\frac{1}{\sqrt{k_B 4\varepsilon\sigma_{\mathrm{SB}}T^3}} \\ &= \frac{\varepsilon}{4\sqrt{\varepsilon k_B \sigma_{\mathrm{SB}}T^5}} \\ D^\star_{\mathrm{J}} &= 1.81\cdot 10^8 \frac{\mathrm{m\ Hz^{1/2}}}{\mathrm{W}} = 1.81\cdot 10^{10}\ \mathrm{Jones} \end{aligned} \tag{S16}$$

### S3.3 M-factor

Dillner *et al.* introduced a dimensionless factor $M$ that connects the $D^\star_{\mathrm{T}}$ to specific detectivity $D^\star_0$ $\left(D^\star_0 = \sqrt{M/(M+1)}D^\star_T\right)$. In other words, if $M$ is sufficiently large, the electrical limitations will be small and the detectivity is mainly thermally limited. In this section we estimate how large $M$ can theoretically be in organic bolometers and how close we can get to the Jones limit. The M-factor can be calculated as:[27]

$$\begin{aligned} M &= \frac{\zeta^2 T}{RG} \\ &= \frac{\alpha^2 U^2 T}{RG} \\ &= \frac{\alpha^2 U^2 T}{R}\frac{\tau}{C} \\ &= \frac{\alpha^2 U^2 T}{R}\frac{\tau}{c_s m} \\ &= \frac{\alpha^2 U^2 T}{R}\frac{\tau}{c_s \rho V} \\ &= \frac{\alpha^2 U^2 T}{R}\frac{\tau}{c_s \rho L^2 d} \\ M &= \left(\frac{\alpha U}{L}\right)^2 \frac{T}{R}\frac{\tau}{c_s \rho d} \end{aligned} \tag{S17}$$

where we take the resistance $R$ = 400 kΩ, $L$ = 400·10$^{-6}$ m, $d$ = 1500·10$^{-9}$ m, $\alpha$ = 2.3 %/K, and $U$ = 10V based on the real samples and we use $\tau$ = 207 ms and 103 ms respectively for $\gamma$ = 0 and $\gamma = 4T_b^3\varepsilon\sigma_{\mathrm{SB}}$ from the calculations in Section 2.3.

$\underline{\gamma = 0}$

$$M \approx \left( \frac{0.023 \frac{1}{\mathrm{K}} \cdot 10\mathrm{V}}{400 \cdot 10^{-6}\mathrm{m}} \right)^2 \cdot \frac{300\mathrm{K}}{400\mathrm{k}\Omega} \frac{207 \cdot 10^{-3}\mathrm{s}}{1100 \frac{\mathrm{kg}}{\mathrm{m}^3} \cdot 770 \frac{\mathrm{J}}{\mathrm{kgK}} \cdot 1500 \cdot 10^{-9}\mathrm{m}}$$
$$\approx 40.4$$

$\underline{\gamma = 4T_b^3 \varepsilon \sigma_{\mathrm{SB}}}$

$$M \approx \left( \frac{0.023 \frac{1}{\mathrm{K}} \cdot 10\mathrm{V}}{400 \cdot 10^{-6}\mathrm{m}} \right)^2 \cdot \frac{300\mathrm{K}}{400\mathrm{k}\Omega} \frac{103 \cdot 10^{-3}\mathrm{s}}{1100 \frac{\mathrm{kg}}{\mathrm{m}^3} \cdot 770 \frac{\mathrm{J}}{\mathrm{kgK}} \cdot 1500 \cdot 10^{-9}\mathrm{m}}$$
$$\approx 20.2$$

from Equation S14

$\underline{\gamma = 0}$

$$D_{\mathrm{T}}^{\star} = \frac{1}{2 \cdot 300\ \mathrm{K}} \sqrt{\frac{207 \cdot 10^{-3}\ \mathrm{s}}{1.39 \cdot 10^{-23} \cdot 1100 \frac{\mathrm{kg}}{\mathrm{m}^3} \cdot 770 \frac{\mathrm{J}}{\mathrm{kgK}} \cdot 1500 \cdot 10^{-9}\mathrm{m}}}$$
$$= 1.78 \cdot 10^{10}\ \text{Jones}$$

$\underline{\gamma = 4T_b^3 \varepsilon \sigma_{\mathrm{SB}}}$

$$D_{\mathrm{T}}^{\star} = \frac{1}{2 \cdot 300\ \mathrm{K}} \sqrt{\frac{103 \cdot 10^{-3}\ \mathrm{s}}{1.39 \cdot 10^{-23} \cdot 1100 \frac{\mathrm{kg}}{\mathrm{m}^3} \cdot 770 \frac{\mathrm{J}}{\mathrm{kgK}} \cdot 1500 \cdot 10^{-9}\mathrm{m}}}$$
$$= 1.26 \cdot 10^{10}\ \text{Jones}$$

Since the $M$'s are so large, we can get the specific detectivities very close to the thermally limited specific detectivities $D_0^{\star} = 0.9878 \cdot D_T^{\star}$ and $D_0^{\star} = 0.9761 \cdot D_T^{\star}$ for vacuum and air, respectively. In turn, this means the detectivity values can be extremely close to the Jones limit ($D_J^{\star}$ = 1.81·10¹⁰ Jones). For a more thorough analysis, we can calculate $M$ for different values of $d$ and $L$ (see Figure S6 Table S2 for the parameters used). The procedure is the same as for the experimental results see Section 4.

This analysis shows that increasing the contact spacing ($L$) will increase the $D_0^{\star}$ until a certain point when the $M$ will go down, and the device will no longer be thermally limited. This can be seen in Figure S6d (the full lines are $D_T^{\star}$), and the dashed lines are $D_0^{\star}$, where we see the detectivity increase until the Jones limit (1.81·10¹⁰ Jones) is reached. After reaching this point, $D_T^{\star}$ stays at the Jones limit while $D_0^{\star}$ starts to drop off. This drop in $D_0^{\star}$ can be explained by the decreasing of $M$ (Figure S6a) which brings a decrease in $\sqrt{M/(M+1)}$ (Figure S6b).

To connect the information from these simulations to practical applications, we can outline what is necessary. For instance, a high detectivity combined with a reasonably small pixel size is essential for utilizing an organic bolometer in thermal cameras. Typically, pixel sizes are around 10 μm. In reference Figure S6, we observe that for a thickness below 1000 nm, we can achieve detectivities of approximately 10⁹ Jones.

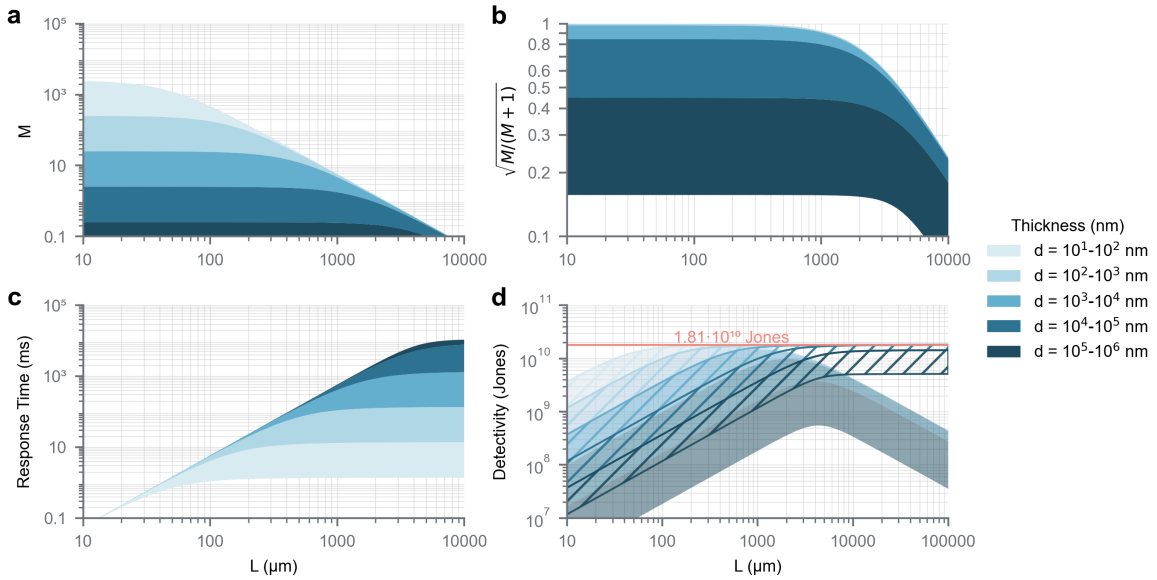


**Figure S6.** (a) $M$ values in function of $L$ for different thicknesses, showing that decreasing the thickness and $L$ significantly increases $M$. (b) $\sqrt{M/(M+1)}$ in function of $L$ for various thicknesses, showing that when $R = 60$ kΩ, $L \leqslant 1000$ µm, and $d \leqslant 1000$ nm $D_0^\star \approx D_T^\star$. (c) The response time shows again that making the devices thinner and the contact spacing shorter is better as it decreases the response time. (d) Detectivity in function of $L$ for various thicknesses: the red line is the the Jones limit ($1.81{\cdot}10^{10}$ Jones). The arced area represents $D_T^\star$, indicating that both reducing the thickness and increasing the contact spacing move $D_T^\star$ closer to the Jones limit. The colored area represents $D_0^\star$. $D_0^\star$ increases toward the Jones limit as the contact spacing increases until approximately $L \approx 3000$ µm, at which point it begins to decrease because electrical noise becomes significant.

**Table S2.** Parameters of investigation of the influence of $d$ and $L$ on $M$ and $D_0^\star$.

| **Parameter** | **Value** |
|---|---|
| $T_b$ | 300 K |
| $k$ | 0.084 W/mK |
| $\rho$ | 1100 kg/m³ |
| $c_s$ | 770 J/kgK |
| $\sigma_{SB}$ | $5.67{\cdot}10^{-8}$ W/m²K⁴ |
| $k_B$ | $1.380649 \cdot 10^{-23}$ J/K |
| $Q_A$ | 1 W/m² |
| $\varepsilon$ | 1 |
| $d$ | 10 nm, 100 nm, 1 µm, 10 µm, 100 µm, 1 mm |
| $L$ | $\{L : L = 10^n, n \in \{-5, -4.96, -4.92, ..., -1\}\}$ |
| $f$ | $\{f : f = 10^n, n \in \{-1, -0.95, -0.90, ..., 4\}\}$ |
| $\alpha$ | 2.2 %/K |
| $R$ | 400 kΩ |
| $\gamma$ | 0 W/m²K |

## S4 Procedure to Extract Figures of Merit

To extract the figures of merit $\tau$, $M$, $D_T^\star$, and $D_0^\star$, the following procedure can be followed

1. **Measure the frequency response:**

   Measure the amplitude of the response signal using a modulated light source using a lockin amplifier.[fn1]

2. **Normalize the amplitude:**

   Normalize the response amplitude to enable the extraction of the 3 dB frequency, $f_{3\mathrm{dB}}$. This occurs when the normalized amplitude is $1/\sqrt{2}$.

3. **Calculate the time constant ($\tau$):**

   Use the relation:

   $$\tau = \frac{1}{2\pi f_{3\mathrm{dB}}}$$

4. **Calculate the thermally limited detectivity ($D_T^\star$):**

   Apply

   $$D_T^\star = \varepsilon D_{\mathrm{Tel}}^\star$$

   to Equation S14

   $$D_{\mathrm{Tel}}^\star = \frac{1}{2T}\sqrt{\frac{\tau}{k_B c_S \rho d}}$$

   to get $D_T^\star$.

   $$D_{\mathrm{T}}^\star = \frac{\varepsilon}{2T}\sqrt{\frac{\tau}{k_B c_S \rho d}}$$

5. **Calculate the electric noise factor:**

   Use Equation S17

   $$M = \left(\frac{\alpha U}{L}\right)^2 \frac{T}{R}\frac{\tau}{c_s \rho d}$$

   to determine the electrical noise contribution $M$.

6. **Calculate the specific detectivity $D_0^\star$:**

   Finally, compute the overall specific detectivity using:

   $$D_0^\star = \sqrt{\frac{M}{M+1}} D_T^\star$$

   to calculate $D_0^\star$.

[fn1] For the simulation the amplitude of the response signal is the $\Delta T_{\max}(f)$

**S5 Spectral Corrections**

When using a Fourier transform infrared (FTIR) spectrometer in continuous mode, the light is modulated by moving one of the mirrors at a constant velocity ($v_{\mathrm{mirror}}$). The difference in the optical path ($\delta$) is proportional to time, which results in the wavenumber ($\sigma$) being proportional to the temporal frequency $f$ after the Fourier transformation:

$$f = 2v_{\mathrm{mirror}}\sigma$$

Often, the mirror velocity is expressed as a frequency ($f_{\mathrm{mirror}}$), and then the equation becomes:

$$f = \frac{f_{\mathrm{mirror}}\sigma}{\sigma_{\mathrm{laser}}} \tag{S18}$$

where $\sigma_{\mathrm{laser}}$ is the wavenumber of the guide laser. The measured signal $M(\sigma)$ can be written as:

$$M(\sigma) = F(f)S(\sigma)I_{\mathrm{lamp}}(\sigma) \tag{S19}$$

Here, $F(f)$ is the frequency response of the detector used for the measurement, $S(\sigma)$ is the actual response of the detector, and $I_{\mathrm{lamp}}(\sigma)$ is the intensity spectrum of the lamp.

In typical transmission measurements, the frequency response of the detector is not critical, as it remains consistent for both the baseline measurement of the lamp and the measurement with the sample. However, during Fourier-transform photocurrent spectroscopy (FTPS) measurements, the baseline measurement of the lamp is conducted with the internal deuterated triglycine sulfate (DTGS) detector, while the sample measurement is performed with a different sample detector. Referencing previous analyses, when we measure $M(\sigma)$ and seek to find $S(\sigma)$, we need the frequency response of the detector. This can be measured using a modulated light source. Additionally, the lamp spectrum can be obtained using the internal DTGS detector, as is standard in regular FTIR measurements. Thus we have:

$$\begin{aligned} M_{\mathrm{DTGS}}(\sigma) &= F_{\mathrm{DTGS}}(f)S_{\mathrm{DTGS}}(\sigma)I_{\mathrm{lamp}}(\sigma) \\ I_{\mathrm{lamp}}(\sigma) &= \frac{M_{\mathrm{DTGS}}(\sigma)}{F_{\mathrm{DTGS}}(f)S_{\mathrm{DTGS}}(\sigma)} \end{aligned} \tag{S20}$$

Fortunately, DTGS detectors exhibit a very flat response due to their pyroelectric properties, allowing us to assume that $S_{\mathrm{DTGS}}$ is constant. Only the frequency response of the DTGS detector needs to be determined. This can be done similarly to the sample detectors using a modulated light source; however, this requires dismantling the FTIR setup. A simpler approach is to measure $M_{\mathrm{DTGS}}$ for different values of $f_{\mathrm{mirror}}$ and use this data to extract the frequency response. By combining Equation S19 and Equation S20 we arrive at the equation:

$$S_{\mathrm{sample}}(\sigma) = \frac{M_{\mathrm{sample}}(\sigma)F_{\mathrm{DTGS}}(f)}{M_{\mathrm{DTGS}}(\sigma)F_{\mathrm{sample}}(f)} \tag{S21}$$

## S6 Synthesis and characterization of PBiTTQHD

Reagents and chemicals were obtained from commercial sources and used without further purification. Solvents were dried by a solvent purification system (MBraun, MB-SPS-800) equipped with alumina columns. 4,9-Dibromo-6,7-bis(5-(2-hexyldecyl)thiophen-2-yl)[1,2,5]thiadiazolo[3,4-g]quinoxaline (**1**) was synthesized according to a literature procedure.[12]

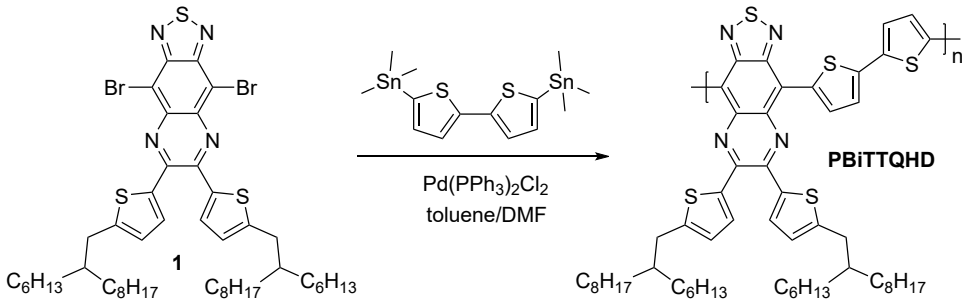


PBiTTQHD. TQ monomer **1** (100 mg, 0.104 mmol), 5,5′-bis(trimethylstannyl)-2,2′-bithiophene (51.2 mg, 0.104 mmol) and $Pd(PPh_3)_2Cl_2$ (1.80 mg, 2.05 µmol) were combined in a Schlenk tube and dissolved in a mixture of dry toluene (0.9 mL) and DMF (0.3 mL), degassed with $N_2$ for 15 min prior to addition. The Schlenk tube was put under nitrogen atmosphere, heated to 120 °C, and the polymerization mixture was stirred overnight. Then, the viscous solution was diluted in chlorobenzene after which diethylammonium diethyldithiocarbamate (20 mg) was added and the mixture was stirred at 100 °C for 1 h. The resulting mixture was then added dropwise to methanol, filtered in a Soxhlet thimble, and purified by repetitive Soxhlet extractions using methanol, acetone, *n*-hexane, methylene chloride, chloroform, and chlorobenzene. The chlorobenzene fraction obtained from Soxhlet extraction was added to a small amount of methanol and the polymer precipitate was filtered off, yielding a dark brown solid (57.8 mg, 57%). SEC: $M_n$ = 6.0 kg/mol, Đ = 2.1. UV-VIS-NIR: $\lambda_{\text{max IR, film}}$ = 1238 nm.

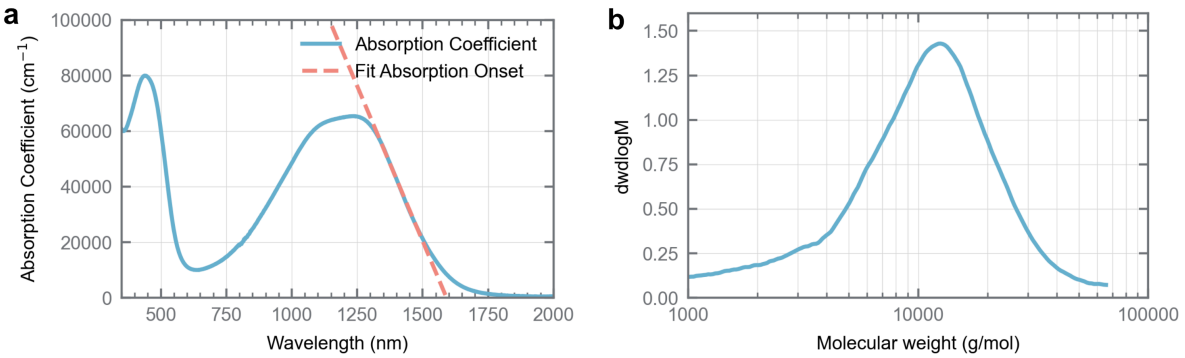


**Figure S7.** (a) Absorption coefficient for the PBiTTQHD polymer in film on glass with absorption onset fit. (b) SEC data showing the molecular weight distribution.

## S7 Finite Element Simulations

### S7.1 Lateral Heat Loss

The 1D heat transfer model presented in Section 2 is valid only when lateral heat loss at the contact edges is minimal. To confirm this, we conducted finite element simulations in COMSOL, examining a range of contact widths and spacings. Our results, shown in Figure S8, demonstrate that for the specific dimensions of our bolometer samples (2 mm contact width and 200 or 400 µm contact spacing), lateral heat loss is negligible (Figure S8c). This finding supports the use of a more simple, analytical model for the device geometry presented in this paper. However, for devices with more square-shaped pixels, where lateral heat transfer becomes more significant, a 2D model would be more appropriate.

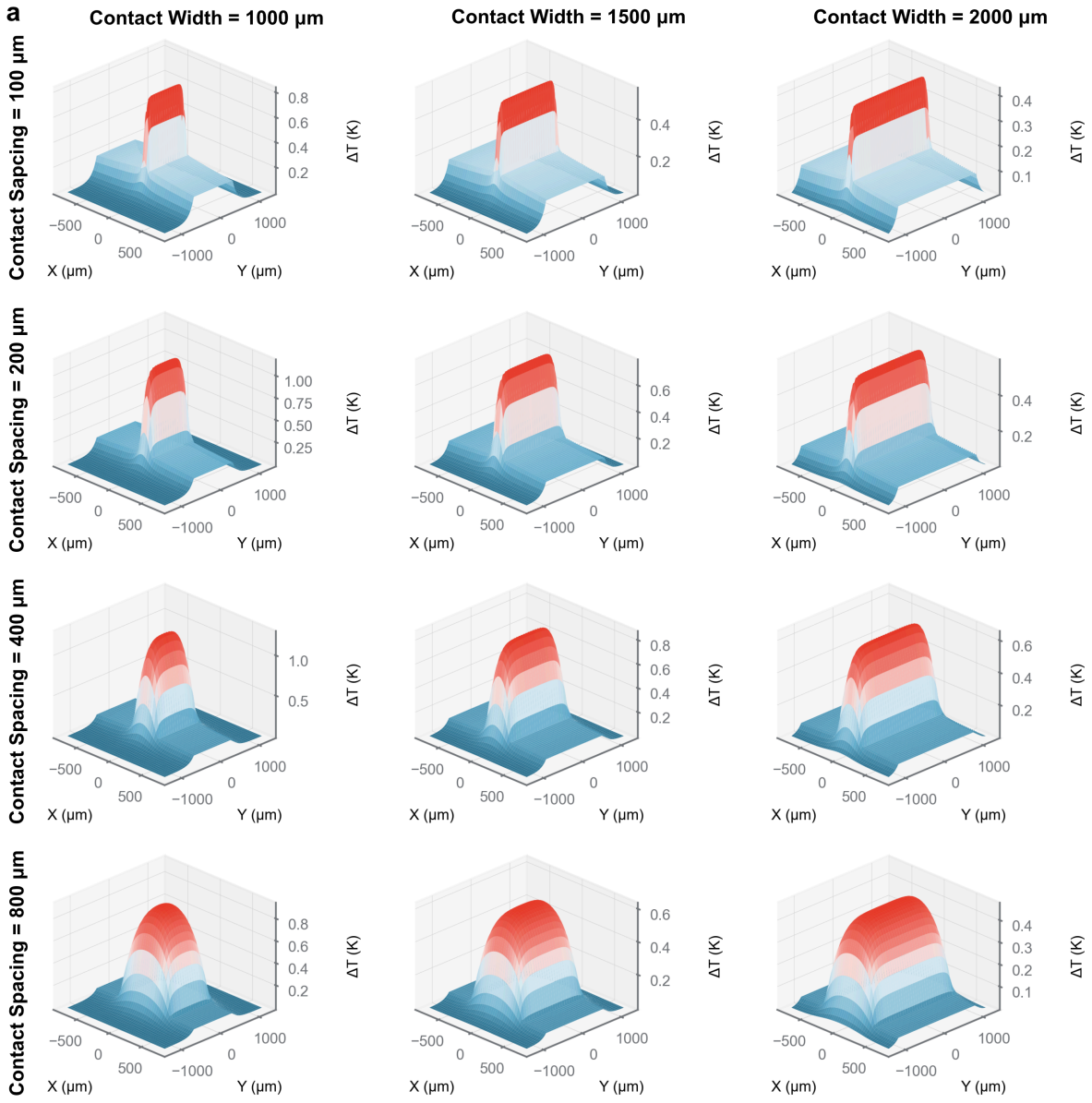

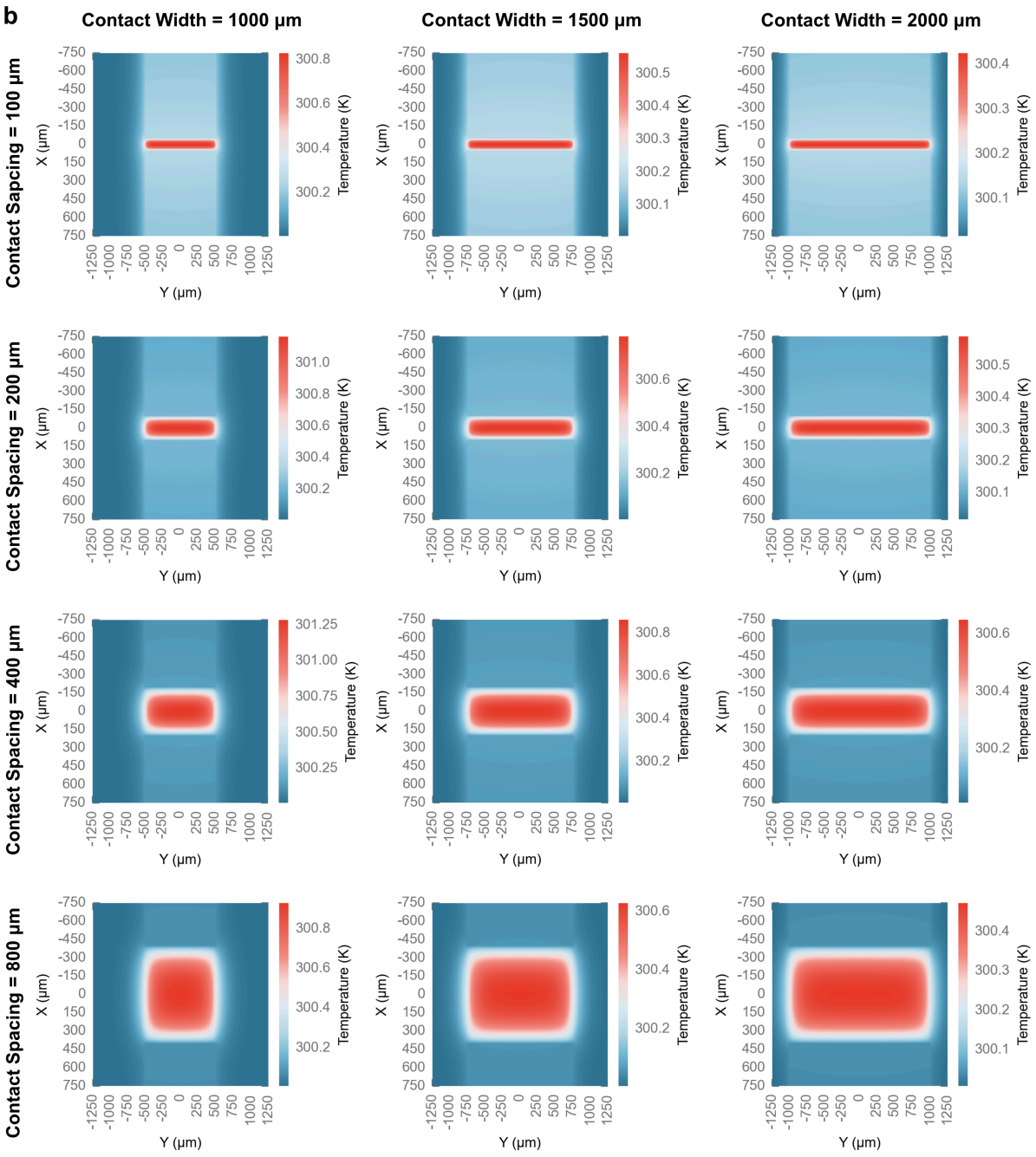
b
Contact Width = 1000 µm
Contact Width = 1500 µm
Contact Width = 2000 µm
Contact Sapcing = 100 µm
Contact Spacing = 200 µm
Contact Spacing = 400 µm
Contact Spacing = 800 µm
X (µm)
Y (µm)
Temperature (K)

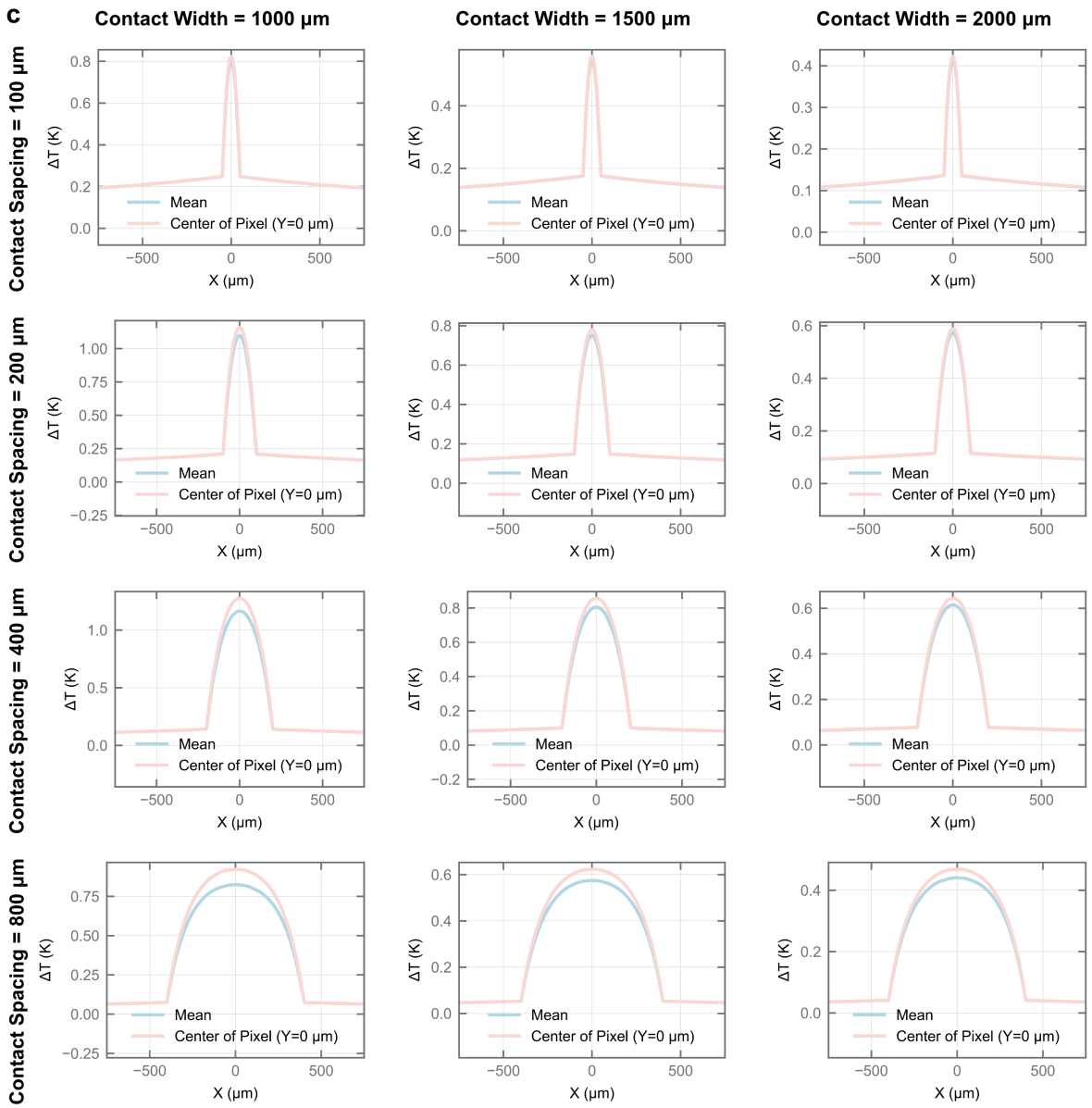


**Figure S8.** Finite Element Simulations of Heat Distribution. **(a)** 3D plots, **(b)** heatmaps, and **(c)** slices of the center and averages over the contact widths from COMSOL simulations showing the effect of contact width and spacing on lateral heat loss. The results confirm that for the dimensions used in our bolometer samples (2 mm contact width and 200/400 µm contact spacing), lateral heat loss is minimal, validating the use of a 1D heat transfer model.

### S7.2 Contact Material and Thickness

To ensure our choice of 100 nm-thick silver contacts did not significantly influence heat transfer, we conducted finite element simulations in COMSOL. The simulations, which varied contact thickness from 50 nm to 400 nm and compared silver with aluminum, revealed no discernible difference in performance. This confirms that both the contact material and thickness have a negligible effect on the device's thermal behavior.

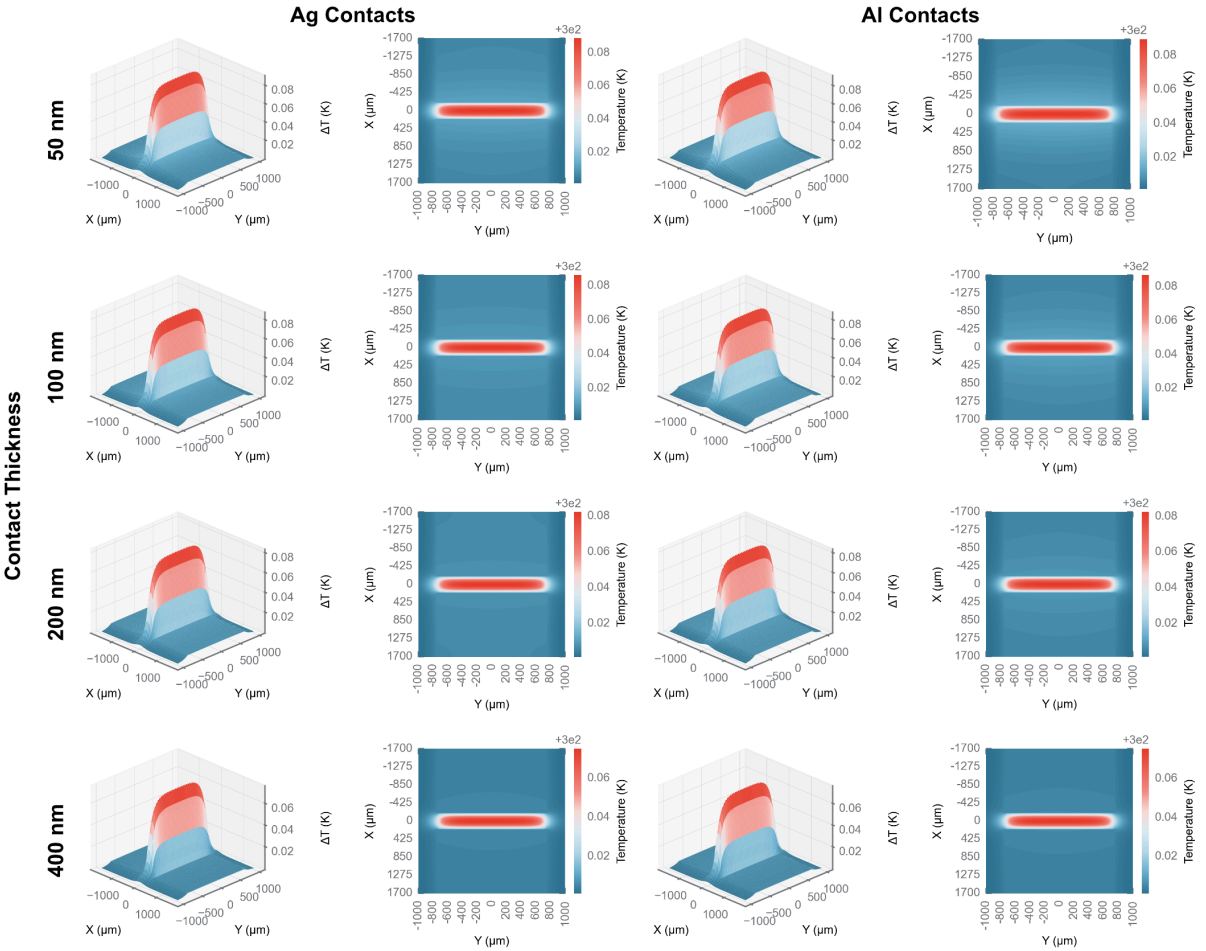


**Figure S9.** 3D plots and heatmaps from COMSOL simulations showing the thermal behavior of devices with varying contact materials and thicknesses. The results demonstrate that the thermal performance is negligibly affected by the choice of contact thickness (50-400 nm) or material (silver vs. aluminum).

### S7.3 Crosstalk

To verify the feasibility of 10 μm pixels and confirm that thermal crosstalk is not a significant issue, we performed finite element simulations in COMSOL. The simulations were conducted both with and without contacts to investigate their impact on heat distribution.

When contacts are present, the heat profile remains confined to the area between the contacts as expected, with most of the residual heat being extracted by the contacts themselves. The temperature drops significantly in the organic material next to the pixel, as shown in Figure S10a and b. Conversely, when no contacts are present, the heat remains largely localized with a steep

temperature drop around the pixel border (Figure S10c and d). These results indicate that thermal crosstalk is minimal, supporting the possibility of small pixelsizes.

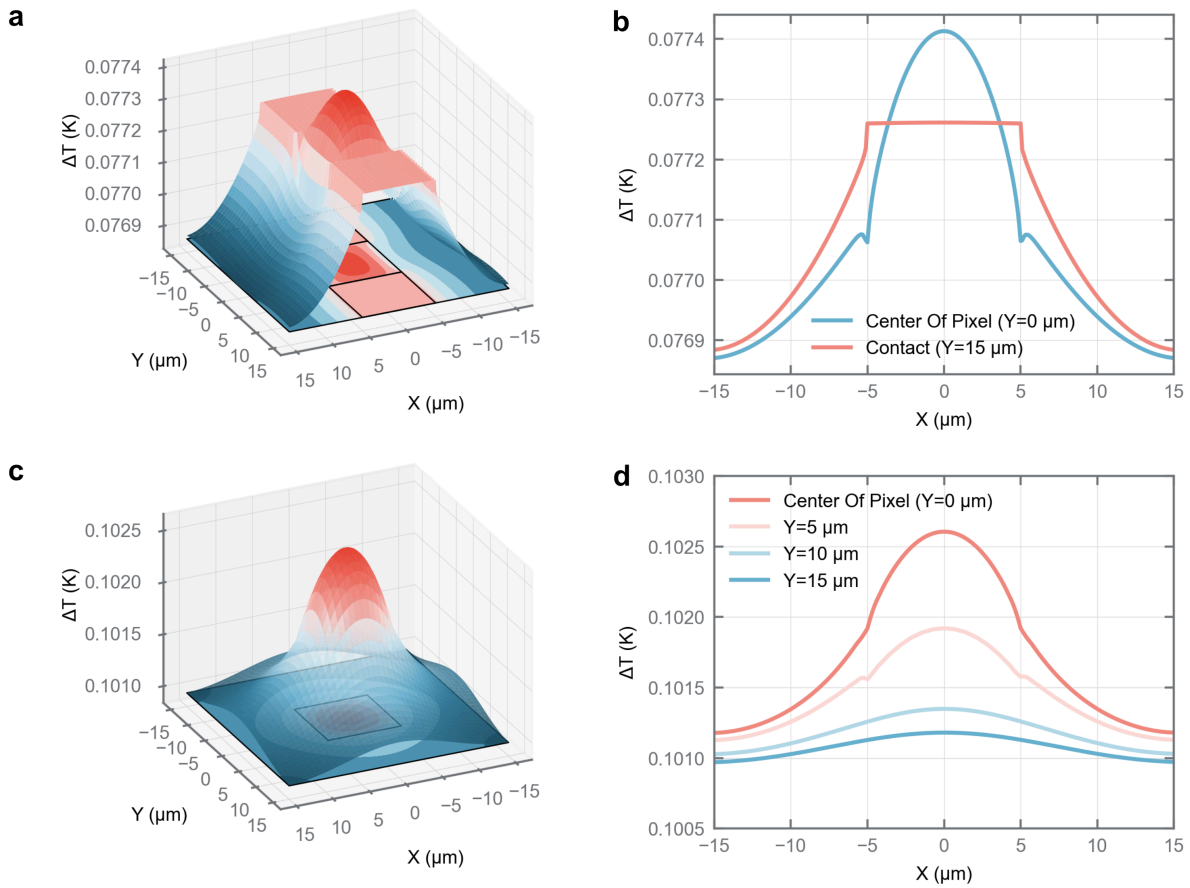


**Figure S10.** (a) 3D plot and projected heatmap showing the heat profile in a pixel with contacts. The heat is largely confined to the area between the contacts, with most excess heat extracted through the contacts. (b) Cross-sectional temperature profiles along the x-direction, taken at the center of the pixel and at the end of the contact. A significant temperature drop is observed in the region where neighboring pixels would be, confirming minimal thermal crosstalk. (c) 3D plot and projected heatmap of a pixel without contacts. The heat profile remains mostly localized, with a sharp temperature drop at the pixel border (10 μm). (d) Cross-sectional temperature profiles along the x-direction. The plot includes slices at the center of the pixel, the pixel border (5 μm), the center of the neighboring pixel (10 μm), and the border of the neighboring pixel (15 μm), further illustrating the localized heat distribution.

## S8 Absorbance Spectra

### S8.1 Evidence of Doping in PBiTTQHD

We successfully doped a PBiTTQHD film using a submersion technique. Initial evidence for successful doping was a distinct color change in the film after a 10-second submersion in an acetonitrile F6TCNNQ solution (Figure S11a).

To quantitatively confirm this visual observation, we measured the absorbance spectra of the film before and after submersion (Figure S11b). The results showed a significant five-fold increase in infrared absorption, which confirms that the doping process was effective. The most

compelling evidence of successful doping was the significant increase in electrical conductivity, which rose by a factor of 18.6 after the submersion treatment (Figure S11c).

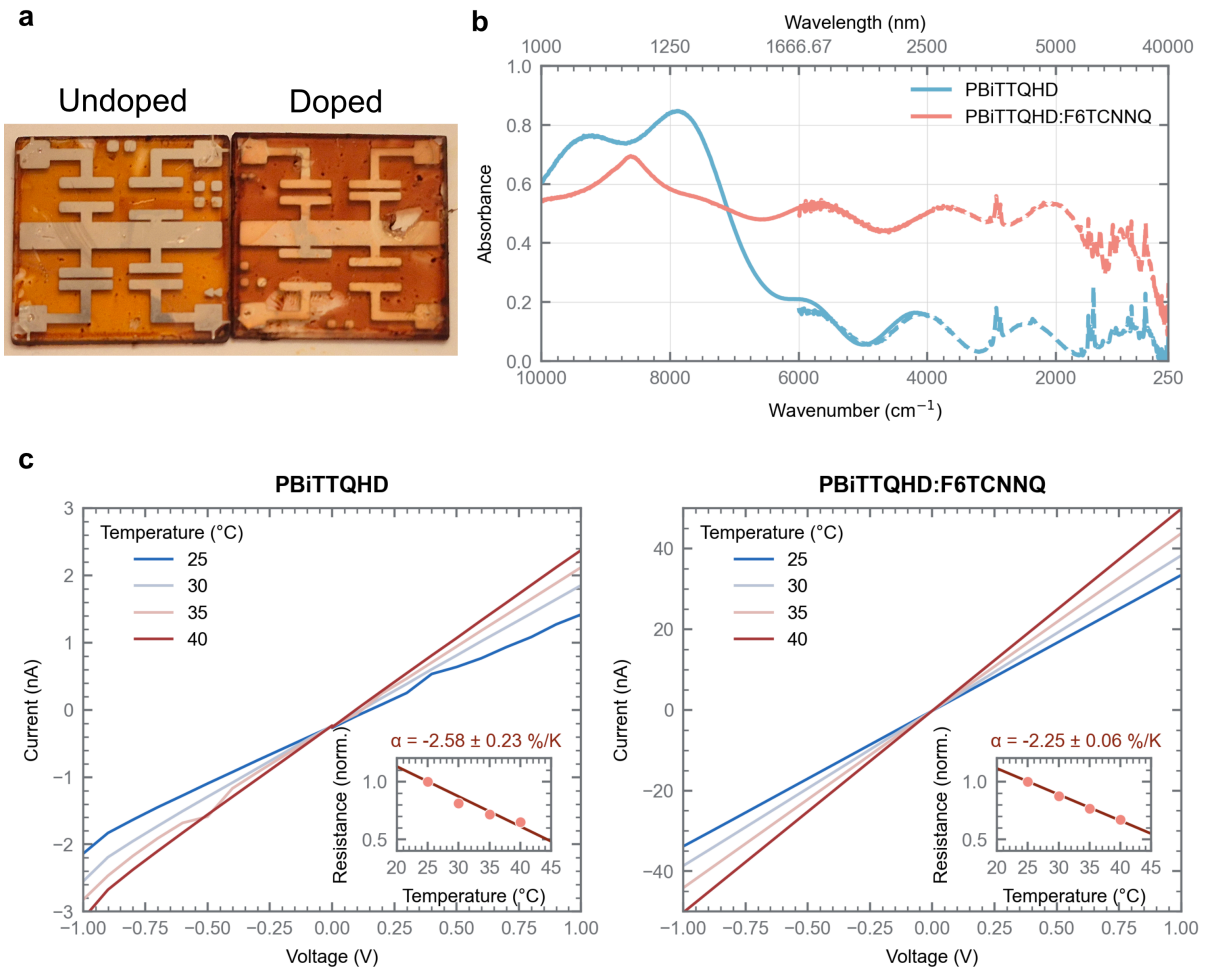


**Figure S11.** (a) A visual comparison of undoped and doped PBiTTQHD, showing the color shift that provides an initial indication of successful doping. (b) Absorption spectra of undoped and F6TCNNQ-doped PBiTTQHD. The substantial increase in infrared absorption confirms the success of the doping procedure. (c) Comparison of the conductivity of undoped and doped PBiTTQHD.

### S8.2 Absorbance Spectra of the Three Material systems

The absorbance spectra for the three material systems MeO-TPD:F6TCNNQ, PBiTTQHD:F6TCNNQ, and PEDOT:PSS, are shown in Figure S12a, b, and c, respectively. All three systems exhibit absorption in the infrared region, with distinct vibrational peaks that correspond to features observed in the main text's response spectra.

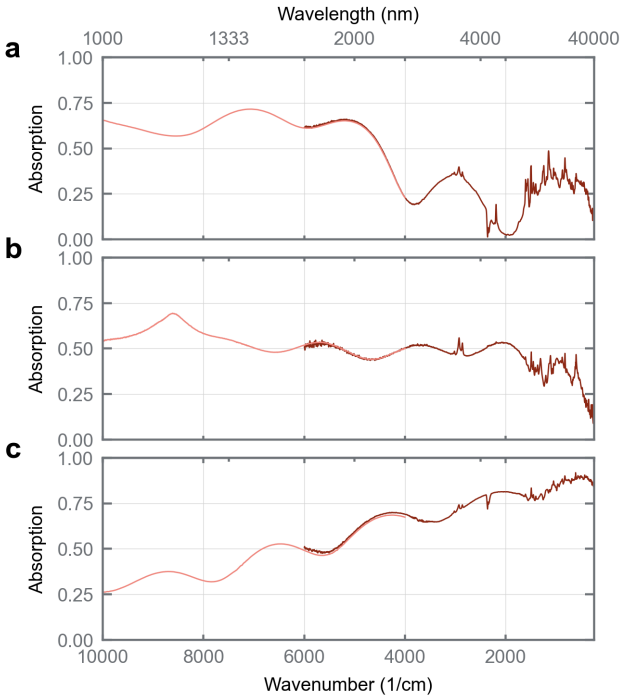


**Figure S12.** Absorbance spectra for (a) MeO-TPD:F6TCNNQ, (b) PBiTTQHD:F6TCNNQ, and (c) PEDOT:PSS. All materials show significant absorption in the infrared region, including vibrational peaks that correlate with the device response spectra.

### S9 Individual Frequency Response Spectra

Figure 3 in the main text shows the average frequency response spectra over multiple samples. The individual spectra for each sample are presented in Figure S13. Each spectrum includes both a forward and a backward frequency scan, with each pass consisting of 10 measurement points at every frequency. The red line in the figure represents a fit of the 1D model to the experimental data.

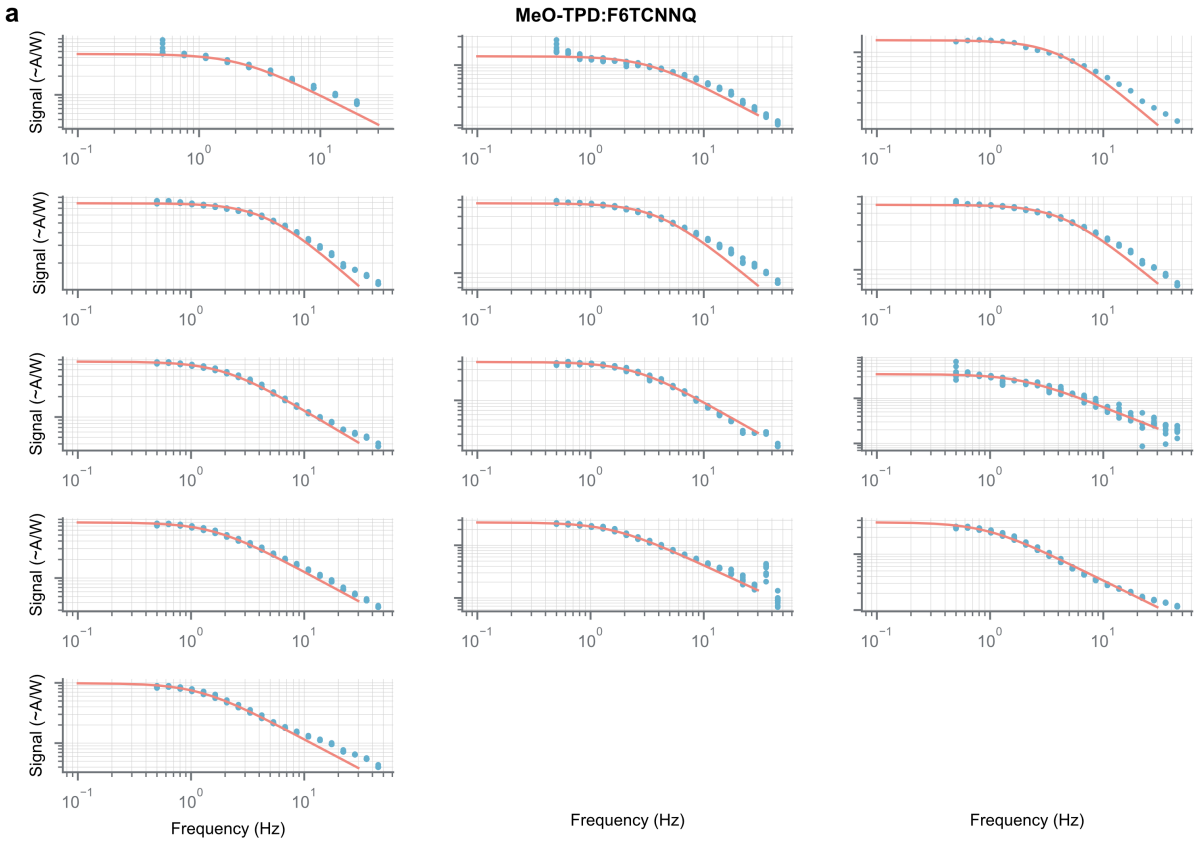
a
MeO-TPD:F6TCNNQ
Signal (~A/W)
Frequency (Hz)
Frequency (Hz)
Frequency (Hz)

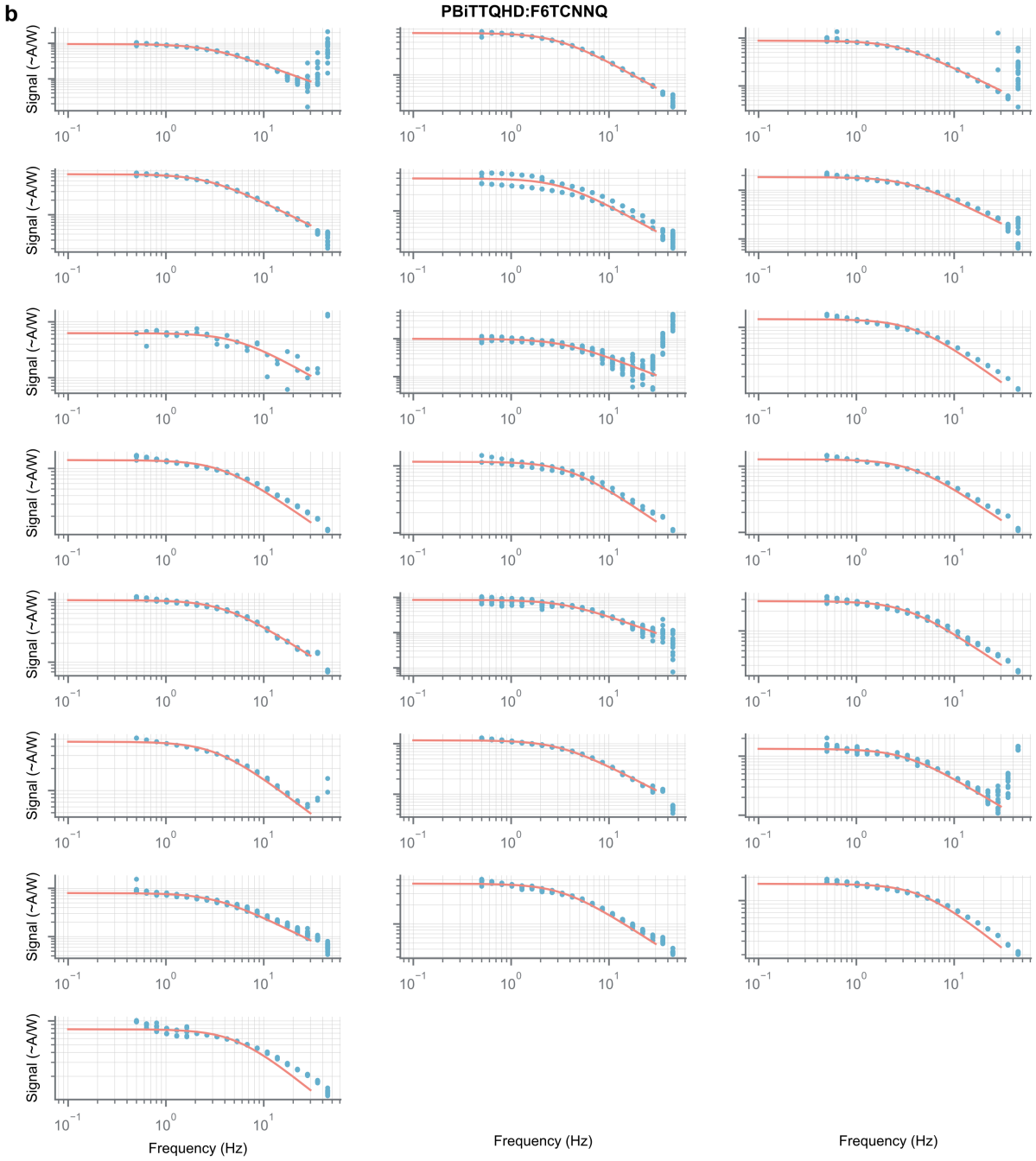
b
PBiTTQHD:F6TCNNQ
Signal (~A/W)
Frequency (Hz)
Frequency (Hz)
Frequency (Hz)

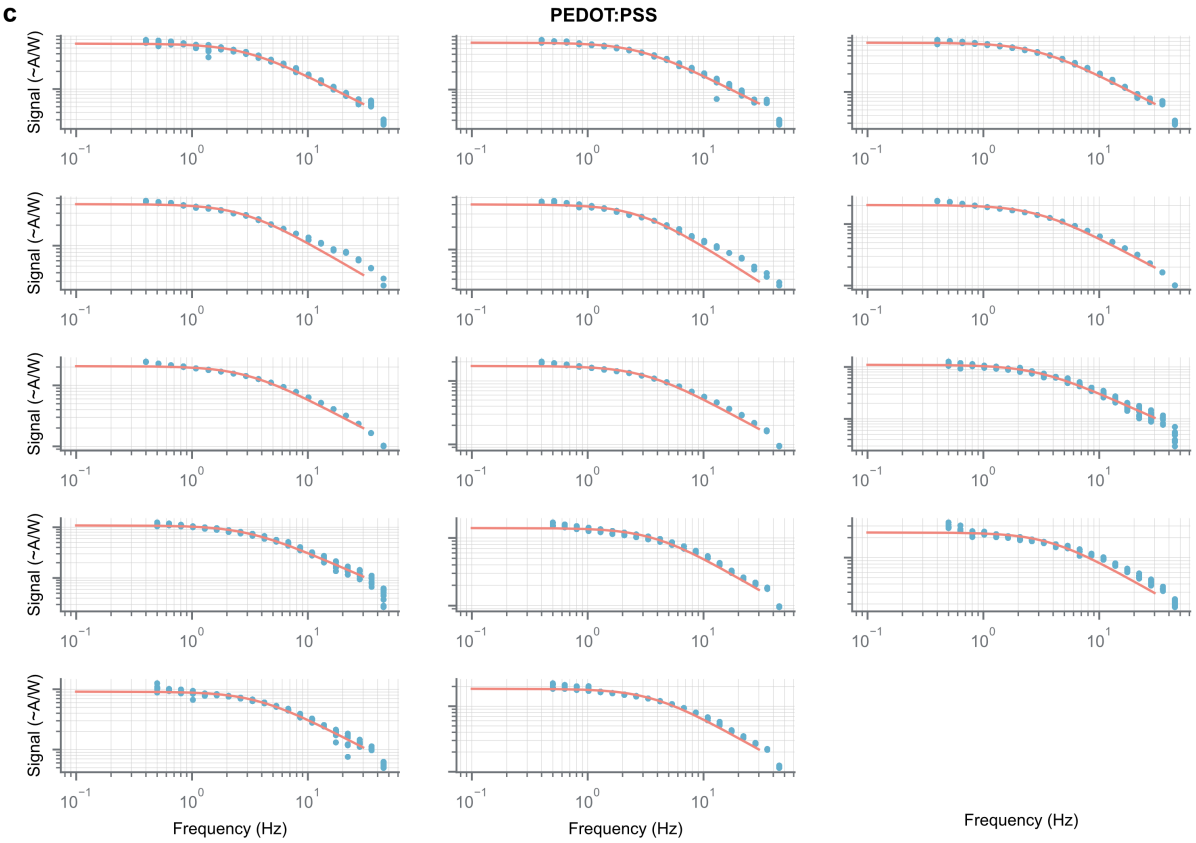


**Figure S13.** Frequency response spectra for individual samples of (a) MeO-TPD:F6TCNNQ, (b) PBiTTQHD:F6TCNNQ, and (c) PEDOT:PSS. Each spectrum includes both a forward and backward scan, with the red line showing a fit of the 1D model to the experimental data.